Nanoscale Advances

ROYAL SOCIETY OF CHEMISTRY

PAPER

View Article Online
View Journal

Cite this: DOI: 10.1039/d5na00962f

Mechanistic insights into vacancy-driven activation and dissociation of hydrogen peroxide on $Ti_3C_2O_2$ MXene in water

Masoud Darvish Ganji [ab] and Hyunseok Ko [*b]

The rational design of sophisticated oxidation and electrochemical systems depends on an understanding of how hydrogen peroxide (H_2O_2) activates and dissociates on two-dimensional catalysts. Here, using a combination of density functional theory (DFT), nudged elastic band (NEB) calculations, electron localization function (ELF) analysis, and machine-learned interatomic potential molecular dynamics (MLIP-MD) simulations we present a thorough multiscale computational study of the H_2O_2 interaction with pristine and oxygen-deficient $Ti_3C_2O_2$ MXene. Using the r^{2}SCAN meta-GGA functional, structural and adsorption properties were carefully investigated and compared to hybrid HSE06 and PBE + *U* simulations. Oxygen vacancies significantly increase surface reactivity by stabilizing firmly bound molecular peroxide intermediates through direct coordination with undercoordinated Ti centers, whereas pristine $Ti_3C_2O_2$ shows poor molecular adsorption of H_2O_2 without O–O bond activation. In contrast to the artificial overbinding and spontaneous dissociation predicted by PBE + *U*, r^{2}SCAN offers a balanced description of Ti–O coordination and peroxide intramolecular bonding, according to the electronic structure and ELF analyses. NEB calculations using the MLIP-CHGNet framework reveal an exceptionally low-barrier, stepwise dissociation pathway at oxygen vacancy sites, where peroxide activation is controlled by surface-assisted stabilization instead of direct bond dissociation. The MLIP-MD simulations were run in an explicit aquatic environment at 300 K in order to capture finite-temperature and solvent effects. These simulations show that explicit water molecules and temperature fluctuations greatly speed up peroxide dissociation, facilitate proton transfer, and stabilize reaction intermediates through hydrogen-bond networks, resulting in quick O–O bond cleavage and H_2O production. Together, these findings demonstrate the importance of explicit solvation and finite-temperature dynamics in controlling peroxide reactivity on MXene surfaces and establish oxygen-defective $Ti_3C_2O_2$ as an effective catalyst for H_2O_2 activation.

Received 10th October 2025
Accepted 2nd April 2026

DOI: 10.1039/d5na00962f

rsc.li/nanoscale-advances

1. Introduction

In a variety of biological and technological systems, hydrogen peroxide (H_2O_2) is a highly reactive oxygen species that can be both a useful oxidizing agent and a hazardous consequence. Because of its role in redox chemistry, it is now a key chemical in a variety of domains, including environmental engineering, nuclear energy, medicinal applications, and heterogeneous and photocatalysis.[1–11] Promoting or suppressing H_2O_2 production and reactivity may be the aim, depending on the system. For example, water radiolysis in nuclear reactors produces H_2O_2, which corrodes and degrades structural materials.[3] The same is true for proton exchange membrane (PEM) fuel cells, where H_2O_2 is an unwanted intermediate of the oxygen reduction process (ORR) that can cause radical production and degrade the polymer membrane.[8,9] Advanced oxidation techniques, on the other hand, use its oxidative potential to treat and disinfect wastewater.[11]

Therefore, it is essential to comprehend and manage the surface interaction of H_2O_2 with catalytic materials in order to maximize positive results and minimize negative ones. Mechanistically, H_2O_2 can adsorb on surfaces and dissociate into hydroxyl or peroxyl radicals; the existence of electronic or structural defects, surface structure, and chemical composition all have a significant impact on these processes. In the past, a great deal of research has been done on noble metal catalysts for redox processes involving H_2O_2, such as Pt and its alloys.[12–17] However, the hunt for more sustainable and adjustable alternatives has been fueled by problems including high cost, limited long-term stability, and radical-induced degradation.

MXenes, or two-dimensional (2D) transition metal carbides and nitrides, have become a prominent and adaptable class of quantum materials. MXenes combine the strong conductivity

[a]Department of BioNano Technology, Gachon University, 1342 Seongnamdae-ro, Sujeong-gu, Seongnam, Gyeonggi, 13120, Republic of Korea
[b]Division of AI Convergence Research, Korea Institute of Ceramic Engineering and Technology (KICET), Jinju 52851, Republic of Korea. E-mail: hko@kicet.re.kr

and structural tunability of metals with the surface chemical diversity of metal oxides. Their general formula is $M_{n+1}X_nT_x$, where M is a transition metal, X is C or N, and T_x denotes surface terminations such –O, –OH, or –F.[18,19] Because of its high thermodynamic stability, large number of surface-active sites, and improved chemical resistance over –OH and –F-terminated versions, oxygen-terminated $Ti_3C_2O_2$ has drawn a lot of attention among the expanding MXene family.[20,21] As the first MXene with uniform surface termination, homogeneously oxygen-terminated $Ti_3C_2O_2$ was recently synthesized experimentally.[22] This offers a well-defined platform for studying defect-driven catalytic processes.

$Ti_3C_2O_2$ is a viable contender for applications such as gas sensors, electrochemical energy storage, catalysis, and environmental remediation because of its distinct surface chemistry and strong reactivity.[23–25] Nevertheless, because of their relatively inert surface topologies and low density of reactive sites, perfect MXenes frequently continue to exhibit inadequate intrinsic adsorption and catalytic performance, especially for small molecule activation.[26] Additionally, spontaneous H_2O dissociation on bare Ti_3C_2 surfaces has been shown in earlier investigations, highlighting the robust catalytic potential of undercoordinated Ti sites and encouraging research into defect-engineered MXenes.[27] This contrasts with the high intrinsic potential of bare MXene surfaces. Defect engineering, more especially the formation of oxygen vacancies, has been suggested as a powerful method to alter the electrical structure and chemical reactivity of MXenes at the atomic level in order to close this gap and get around the passivating effects of surface terminations.[28–30] Recent experimental and theoretical studies have demonstrated that introducing oxygen vacancies or surface –OH groups dramatically increases the reactivity of $Ti_3C_2O_2$ and similar MXenes, allowing pollutant molecules to dissociate and enhancing catalytic activity.[31]

One effective method for adjusting the catalytic characteristics of two-dimensional materials is defect engineering. Defects can significantly change the catalytic environment by producing localized electronic states, altering the local charge distribution, and promoting charge transfer during adsorption and dissociation processes. Specifically, it has been demonstrated both theoretically and experimentally that oxygen vacancies in $Ti_3C_2O_2$ MXene increase surface reactivity by forming coordinatively unsaturated Ti centers that function as effective electron donor–acceptor sites.[32] However, a fundamental understanding of how these vacancy defects affect reactive oxygen species like hydrogen peroxide's adsorption, activation, and dissociation is still lacking.

Despite the widespread use of density functional theory (DFT) to study surface contacts and reaction energetics, traditional semi-local methods may not adequately describe transition-metal–oxygen interactions due to self-interaction errors.[33,34] Furthermore, finite-temperature and dynamic effects—which are crucial under genuine catalytic conditions—are intrinsically ignored in static DFT calculations.[35,36] It has recently been shown that meta-GGA and hybrid exchange–correlation functionals provide better precision in characterizing transition-metal oxides and defect states in order to overcome these constraints.[37,38] Furthermore, machine-learned interatomic potentials (MLIPs) overcome the computational constraints of conventional *ab initio* molecular dynamics (AIMD) and offer an effective framework for investigating reaction pathways and thermal dynamics with nearly first-principles fidelity.[39,40]

We report a thorough multiscale study of H_2O_2 adsorption and dissociation on both pristine and oxygen-deficient $Ti_3C_2O_2$ ($Ti_3C_2O_2$–O_{vac}) surfaces. In order to guarantee accurate treatment of defect-induced electronic states, the structural, electronic, and adsorption properties are mainly investigated utilizing the r^{2}SCAN meta-GGA functional. The mechanisms of charge redistribution and electron localization that control the activation of O–O bonds are thoroughly examined. Using climbing-image nudged elastic band calculations based on the machine-learning framework, reaction kinetics are investigated, allowing precise mapping of minimum-energy pathways. The stability, reactivity, and dissociation behavior of peroxide under ambient and aqueous conditions are also revealed by means of extensive molecular dynamics (MD) simulations conducted within the MLIP framework to capture finite-temperature effects and explicit solvent interactions.

Through the integration of precise electronic-structure theory and atomistic simulations powered by machine learning, this research offers a cohesive mechanistic comprehension of defect-mediated peroxide activation on MXene surfaces. The knowledge gained elucidates the ways in which oxygen vacancies govern charge transfer, bond activation, and reaction kinetics, providing fundamental guidance for the rational design of catalysts and sensing platforms based on MXene. More generally, this work emphasizes how crucial it is to combine sophisticated DFT techniques with solvated and dynamic simulations in order to do predictive modeling of catalytic processes in realistic environments.

2. Computational methods

All first-principles calculations were performed within the framework of density functional theory (DFT) using the Vienna *Ab initio* Simulation Package (VASP, version 6.3.2).[41–43] The interaction between ionic cores and valence electrons was described using the projector-augmented wave (PAW) method. The primary method for handling exchange–correlation effects was the revised regularized strongly constrained and appropriately normed (r^{2}SCAN) functional, a meta-generalized gradient approximation (meta-GGA), which has been shown to provide better accuracy for surface bonding, adsorption energetics, and defect thermochemistry by lowering density-driven and self-interaction errors that are frequently seen in conventional GGA functionals.

For comparison and validation purposes, additional calculations were performed using the Perdew–Burke–Ernzerhof (PBE) functional,[44] enabling assessment of the performance of widely used GGA-level approaches for the MXene–adsorbate systems under investigation. In systems containing oxygen vacancies, where localized Ti 3d states play a significant role, on-site electron correlation effects were accounted for using the

PBE + U method within the Dudarev formalism.[45] An effective Hubbard parameter of U_{eff} = 3.0 eV was applied to Ti 3d orbitals, consistent with prior studies on Ti-based oxides and MXenes.[46–48]

Selected adsorption configurations, especially those involving oxygen-vacancy-containing MXene surfaces, were recalculated using the screened hybrid functional HSE06 in order to better validate the adsorption capabilities. By providing an extra benchmark, these hybrid functional computations validated the relative stability trends and the resilience of the adsorption geometries predicted by r^{2}SCAN. Conventional PBE + U optimization of the H_2O_2/$Ti_3C_2O_2$ system (≈88 atoms) takes about 384 core-hours per structure in our host high-performance computing (HPC) environment. In comparison, hybrid HSE06 calculations are more than two orders of magnitude slower (100 times more computationally demanding) than PBE + U, whereas r^{2}SCAN calculations are roughly five times more computationally demanding. By contrast, it is notable that the MPIL approach can process these same jobs in just a few hours (~15 core-hours per structure) on

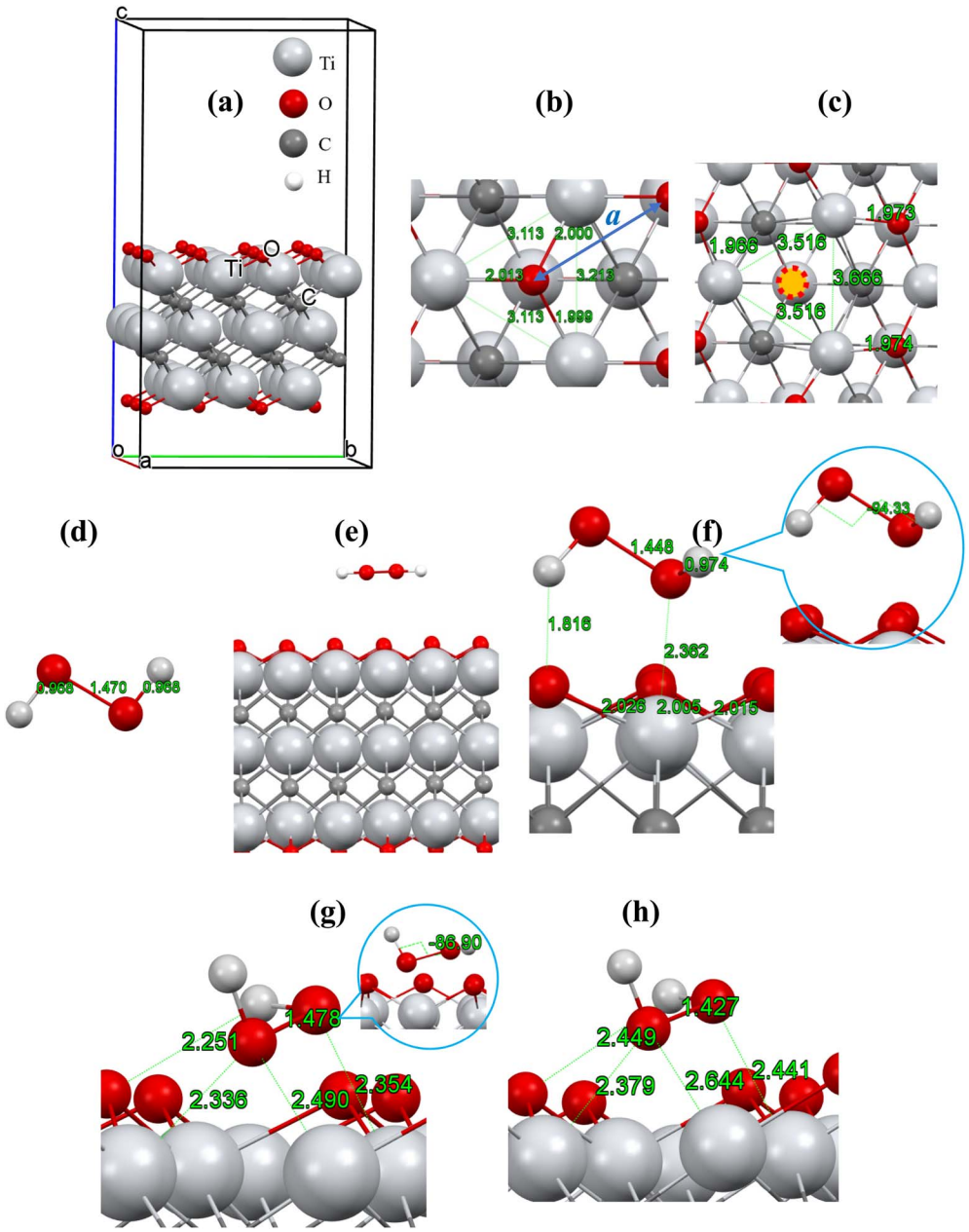

Fig. 1 (a) The initial model for the pristine $Ti_3C_2O_2$ MXene lattice. The lattice vectors a, b, and c are indicated. (b) The optimized structure of the pristine $Ti_3C_2O_2$ MXene surface with r^{2}SCAN. (c) Top view of the oxygen-deficient $Ti_3C_2O_2$ surface, showing the bond lengths of the defective surface. The dotted red line indicates the removed O atom from the surface. (d) The optimized structure of free H_2O_2 molecule. (e) The initial model for H_2O_2 adsorption on the pristine $Ti_3C_2O_2$ surface. (f) The optimized structure of H_2O_2 on the pristine $Ti_3C_2O_2$ surface (the inset shows the distortion of the H–O–O–H dihedral angle). The optimized structure of H_2O_2 on the oxygen-deficient $Ti_3C_2O_2$ surface with (g) r^{2}SCAN (the inset shows the distortion of the H–O–O–H dihedral angle) and (h) hybrid HSE06. Distances are given in angstroms (Å).

a standard Core-i7 PC. Large-scale reaction route discovery is severely limited by the high computing cost of r^{2}SCAN and HSE06, despite the fact that they offer better accuracy in characterizing defect-state localization and adsorption energetics.

2.1 Surface models and DFT setup

Surface properties were modeled using periodic slab representations of $Ti_3C_2O_2$ MXene (Fig. 1a). The rectangular unit cell served as the basis for the construction of an orthorhombic 3 × 2 supercell, with optimal lattice parameters of $a = 9.639$ Å and $b = 10.666$ Å. A total of 86 atoms were present in the slab, including 36 Ti atoms, 24 C atoms (which corresponded to 12 formula units of Ti_3C_2), and 24 surface O atoms, which represented full O termination. Selective removal of surface O atoms from energetically advantageous places produced oxygen-vacancy models. To remove erroneous slab–slab interactions, a vacuum region of at least 20 Å was added along the surface normal (*c*-direction). All atomic positions were fully optimized until the remaining stresses on each atom were less than 0.01 eV Å^{-1}. A plane-wave energy cutoff of 600 eV and a Monkhorst–Pack *k*-point mesh of 3 × 3 × 1 were employed for structural optimizations. Electronic self-consistency was achieved with an energy convergence threshold of 10^{-6} eV.

Interaction properties were analyzed at the r^{2}SCAN level of theory by quantifying charge transfer during adsorption using Bader charge analysis, while changes in chemical bonding were examined *via* electron localization function (ELF) mapping. Electronic structure calculations, including density of states (DOS) and band structures, were likewise performed at the r^{2}SCAN level along high-symmetry paths of the surface Brillouin zone. The band structure was evaluated along the *Γ*–*X*–*S*–*Y* path of the orthorhombic lattice using line-mode *k*-point paths generated with VASPKIT,[49] with 20 *k*-points sampled along each segment to accurately capture defect-induced states near the Fermi level.

2.2 Adsorption energetics

The adsorption and interaction properties of H_2O_2 were systematically investigated by optimizing H_2O_2 adsorption geometries on both pristine and oxygen-defective $Ti_3C_2O_2$ ($Ti_3C_2O_2$–O_{vac}) MXene surfaces at the r^{2}SCAN level of theory. For selected adsorption configurations, PBE + *U* calculations were additionally performed to assess the influence of conventional exchange on adsorption energies. A plane-wave energy cutoff of 600 eV and a Monkhorst–Pack *k*-point mesh of 7 × 7 × 1 were employed for single-point energy calculations. Adsorption energies were computed by referencing the total energies of the isolated slab and H_2O_2 molecule, using consistent computational settings. By designing H_2O_2 adsorption geometries on both pristine $Ti_3C_2O_2$ and $Ti_3C_2O_2$–O_{vac} surfaces at the r^{2}SCAN level of theory, the adsorption and interaction properties of H_2O_2 were methodically examined. PBE + *U* calculations were also carried out for considered adsorption configurations in order to evaluate the impact of conventional exchange on adsorption energies. For single-point energy calculations, a Monkhorst–Pack *k*-point mesh of 7 × 7 × 1 and a plane-wave energy cutoff of 600 eV were used. Using consistent computational parameters, adsorption energies were calculated by referencing the total energies of the isolated slab and H_2O_2 molecule.

The adsorption energy (E_{ads}) of H_2O_2 on the MXene surface was calculated according to

$$E_{ads} = E_{H_2O_2/MX} - E_{MX} - E_{H_2O_2} \quad (1)$$

In this calculation, $E_{H_2O_2/MX}$ represents the total energy of the optimized adsorption system, E_{MX} represents the total energy of the relaxed clean (pristine or oxygen-vacancy-containing) MXene surface, and $E_{H_2O_2}$ represents the total energy of an isolated H_2O_2 molecule computed using the same computational parameters. Exothermic adsorption is indicated by a negative E_{ads}.

2.3 Machine-learned interatomic potential molecular dynamics

MD simulations were conducted employing the CHGNet (Crystal Hamiltonian Graph Network) MLIP to investigate finite-temperature dynamics, solvent effects, and adsorption stability beyond the timescales available to *ab initio* molecular dynamics. A universal machine-learning force field (uMLFF) based on graph neural networks, CHGNet has been trained on extensive density functional theory datasets, allowing for near-*ab initio* accuracy at a fraction of the computational cost.[40] The pre-trained CHGNet model used in all atomistic simulations was trained on the Materials Project Trajectory (MPtrj) dataset, which includes roughly 1.58 million structural frames covering 89 chemical elements, including Ti, C, O, and H—elements that are directly related to $Ti_3C_2O_2$ MXene surfaces and H_2O_2/H_2O adsorbates. Strong chemical transferability is ensured for modeling oxygen-functionalized and oxygen-vacancy-containing MXene systems by including a variety of oxide, surface, defect, and adsorption conditions in the training data.

In order to evaluate the effects of solvent-mediated stabilization, MLIP-MD simulations were performed for H_2O_2 adsorbed $Ti_3C_2O_2$–O_{vac} surfaces under two representative conditions: (i) an isolated H_2O_2 molecule interacting with the $Ti_3C_2O_2$–O_{vac} surface, and (ii) H_2O_2 embedded within an explicit aqueous environment in contact with the $Ti_3C_2O_2$–O_{vac} surface. The Berendsen thermostat as implemented within Atomic Simulation Environment (ASE) was used for all simulations, which were run in the canonical (NVT) ensemble at 300 K. Trajectories were propagated for up to 15 ps to guarantee adequate equilibration and sampling of adsorption behavior, and a time step of 0.5 fs was used to precisely capture hydrogen-related vibrational dynamics.

In comparison to DFT (GGA and GGA + *U*) reference calculations, CHGNet's benchmarked mean absolute errors (MAEs) of roughly 33 meV per atom for total energies and 0.07 eV Å^{-1} for atomic forces support the model's dependability for characterizing H_2O_2/H_2O adsorption, hydrogen bonding, and bond activation processes.[40] These error levels guarantee a faithful representation of the underlying potential energy surface (PES), which is crucial for peroxide species where small changes in

O–O and O–H bonding have a significant impact on reaction pathways. They also fall within the range typically referred to as "chemical accuracy" for surface reaction modeling. Multiple adsorption geometries, surface binding motifs, and solvent-induced rearrangements are just a few examples of the configurational space that can be extensively explored thanks to the transferable nature of the pre-trained CHGNet model at a scale that remains inaccessible to standard *ab initio* molecular dynamics (AIMD). Furthermore, massive supercells of ~180 atoms or more would be needed for full AIMD simulations of the solvated interface. These supercells are computationally inaccessible within standard DFT-based AIMD frameworks for the time scales required to detect reaction completion. However, long-time sampling up to equilibrium conditions (>10 ps) is made possible using CHGNet-based molecular dynamics simulations, which is crucial for capturing solvent-mediated proton transfer and dynamic hydrogen-bond rearrangements that are a part of the H_2O_2 dissociation mechanism. The MD and NEB simulation workflows were built using CHGNet in conjunction with the ASE,[50] and JARVIS-Tools[51,52] were utilized to guarantee consistent and repeatable workflow management.

A validation phase involved using CHGNet to perform zero-temperature relaxations of isolated H_2O_2 adsorbed on pristine $Ti_3C_2O_2$ and $Ti_3C_2O_2$–O_{vac} surfaces. The results were then directly compared with DFT calculations using r^{2}SCAN and HSE06. Consistent adsorption geometries, same preferred binding motifs, and the same relative stability ordering were found in these studies; adsorption attributes varied only within the anticipated accuracy bounds of the most advanced MLIPs. This cross-validation demonstrates the dependability of the MD simulations based on CHGNet for examining reaction pathways and finite-temperature adsorption dynamics.

2.4 Reaction pathway calculations with MLIP-NEB

Reaction pathways for H_2O_2 activation and dissociation on the $Ti_3C_2O_2$–O_{vac} surface were determined using the nudged elastic band (NEB) method at the CHGNet MLIP level. In order to guarantee a well-resolved minimal energy path (MEP), NEB calculations were carried out using the Janus framework[53] with the CHGNet MLIP, utilizing the conventional NEB formulation with a total of 20 intermediate images with a spring constant of 0.1 eV Å^{-2}. Before NEB interpolation, the initial and end states were completely optimized. The ASE interpolator was used in the NEB computations to create intermediate images, and the limited-memory Broyden–Fletcher–Goldfarb–Shanno (LBFGS) optimizer was used to optimize all of the images. Until the greatest residual force on each atom was less than around 0.05 eV Å^{-1}, geometry optimization was carried out. By allowing the highest-energy image to converge toward the saddle point along the reaction coordinate, the climbing-image approach was used to precisely locate transition states. The intricacy of the reaction landscape under a realistic surface was reflected in the hundreds of optimization steps needed to obtain convergence in typical NEB calculations. The main challenge in calculating reaction pathways lies in the large number of intermediate configurations that need to be completely optimized within the NEB framework. When employing sophisticated meta-GGA or hybrid functionals, the overall computing cost becomes unaffordable due to the iterative self-consistent electronic relaxation required for each image. High fidelity to r^{2}SCAN and HSE06 reference energetics is maintained while effective geometry optimization of intermediate states is made possible in this work by the CHGNet machine-learned interatomic potential. The dependability of the MLIP-accelerated technique is validated by the fact that the optimum H_2O_2 adsorption configuration at the oxygen vacancy achieved with CHGNet is in great agreement with r^{2}SCAN and hybrid functional results.

Overall, this multiscale computational framework allows for a thorough and accurate description of H_2O_2 adsorption, activation, and dissociation on pristine and defective $Ti_3C_2O_2$ surfaces under both vacuum and aqueous conditions with CHGNet-based molecular dynamics and NEB reaction pathway analysis.

3. Results and discussion

In this section, we present the key findings from our multi-faceted computational investigation into the interaction of H_2O_2 with pristine and oxygen-deficient $Ti_3C_2O_2$. Our findings offer a thorough understanding of the fundamental principles guiding this process by combining DFT with the r^{2}SCAN/PBE + *U*, electronic structure analysis, and MLIP simulations.

The adsorption characteristics of H_2O_2 on the considered surfaces are first examined, revealing a significant variation in reactivity. The significance of defect states in activating the MXene is then revealed as we examine the electronic structure characteristics of the systems using band structure and DOS analysis. Finally, we offer a thorough examination of the interaction properties by visualizing the bond formation/breaking using ELF analysis and calculating the reaction barrier using the NEB technique. MD-MLIP simulations in a realistic aqueous environment, which reveal the critical function of explicit water molecules in the catalytic process, further corroborate our findings. All of these findings show that the presence of oxygen vacancies changes the MXene from a passive substrate to a very reactive catalyst.

3.1 Adsorption properties

The interaction of H_2O_2 with pristine and oxygen-deficient $Ti_3C_2O_2$ was systematically investigated using the r^{2}SCAN meta-GGA and PBE + *U* approaches (Table 1, Fig. 1 and S1). The r^{2}SCAN functional was employed to reassess the adsorption mechanism due to its improved description of intermediate-range bonding, surface reactivity, and self-interaction effects relative to semi-local GGA functionals. To verify the structural reliability of the employed exchange–correlation functionals, the optimized geometries of the pristine $Ti_3C_2O_2$ lattice obtained with r^{2}SCAN and PBE + *U* (Fig. 1b and S1b) were compared against available experimental data and established literature benchmarks. The experimentally reported in-plane lattice parameters for oxygen-terminated $Ti_3C_2T_x$ MXenes (*a*

Table 1 Interaction energies (E_{int} in eV), adsorption bond lengths ($d_{H_2O_2\cdots MX}$ in Å), and charge transfer for H_2O_2 on pristine and oxygen-vacant ($Ti_3C_2O_2$–O_{vac}) $Ti_3C_2O_2$ surfaces. Results are calculated at the r^{2}SCAN meta-GGA level, with PBE + U values provided in parentheses

Species	E_{int} (eV)	$d_{H_2O_2\cdots MX}$ (Å) "O⋯Ti"	Bader charge (e)
$H_2O_2/Ti_3C_2O_2$	−0.54 (−0.41)	2.362 (2.828)	−0.04 (0.08)
$H_2O_2/Ti_3C_2O_2$–O_{vac}	−1.60 (−5.03)	2.336 (dissociated)	−0.15 (1.13)

≈ 3.03–3.08 Å, depending on termination and synthesis conditions)[54] are in excellent agreement with the r^{2}SCAN-optimized lattice constant for pristine $Ti_3C_2O_2$, which is a = 3.112 Å. Ti–C = 2.180 Å and Ti–O = 2.00 Å are predicted by r^{2}SCAN in accordance with the range deduced from X-ray diffraction and EXAFS investigations of $Ti_3C_2O_2$-rich MXenes (Ti–C ≈ 2.15–2.20 Å, Ti–O ≈ 1.95–2.02 Å). According to these findings, carbide and oxide bonding in the MXene lattice are both structurally balanced described by r^{2}SCAN. These findings suggest that r^{2}SCAN provides a structurally balanced description of both carbide and oxide bonding in the MXene lattice.

In contrast, the PBE + U-optimized pristine structure (Fig. S1b) produces much longer bond lengths (Ti–C = 2.321 Å and Ti–O = 2.03 Å) but a virtually identical lattice constant (a = 3.113 Å). In line with the known propensity of GGA-based functionals with on-site U corrections to over-delocalize bonding in layered carbides, the much longer Ti–C bond indicates an overestimation of lattice softness and decreased metal–carbon covalency, even though the Ti–O distance stays close to experimental estimates.

The introduction of an oxygen vacancy in the $Ti_3C_2O_2$ surface induces local structural reconstruction relative to the pristine lattice (Fig. 1c and S1c). The overall lattice integrity is maintained when a surface oxygen atom is removed, resulting in a small contraction of the Ti–Ti distances and a moderate inward relaxation of the nearby Ti atoms at the r^{2}SCAN level. Without significantly distorting the $Ti_3C_2O_2$ framework, this localized reconstruction shows the creation of coordinatively unsaturated Ti centers. In contrast, PBE + U anticipates more noticeable relaxations surrounding the vacancy, which is in line with its propensity to magnify defect-induced lattice distortions and over-stabilize decreased Ti states.

Overall, the structural parameters that r^{2}SCAN produces for pristine and oxygen-defective $Ti_3C_2O_2$ surfaces are generally closer to experimental values than PBE + U, as seen by these geometric comparisons. A strong basis for interpreting the different adsorption and reactivity patterns of H_2O_2 on the considered substrates covered in the following sections is provided by this enhanced geometric fidelity.

In the initial adsorption models, the H_2O_2 molecule (Fig. 1d) was placed with its molecular axis parallel to the $Ti_3C_2O_2$ surface, orienting the oxygen atoms toward surface Ti sites and the hydrogen atoms toward surface O atoms (Fig. 1e). This configuration allows for both hydrogen bonding and direct Ti–O interactions and enables the system to explore physisorption as well as chemisorption pathways.

3.1.1 Adsorption on pristine $Ti_3C_2O_2$. H_2O_2 adsorbs molecularly on the $Ti_3C_2O_2$ surface without O–O bond cleavage at both the PBE + U and r^{2}SCAN levels. On the other hand, a somewhat stronger interaction is predicted by r^{2}SCAN. The r^{2}SCAN adsorption energy is −0.54 eV, as seen in Table 1, compared to −0.41 eV with PBE + U. Enhanced surface–adsorbate coupling is indicated by a decrease in the equilibrium O(H_2O_2)–Ti distance from 2.83 Å (PBE + U – Fig. S1e) to 2.36 Å (r^{2}SCAN – Fig. 1f). The H–O–O–H dihedral angle is significantly distorted in the optimized r^{2}SCAN geometry (Fig. 1f), going from about 180° in the isolated molecule to about 94°. This facilitates hydrogen bonding between the H_2O_2 hydrogen atoms and the oxygen atoms on the surface. The molecular integrity of H_2O_2 is confirmed by the internal O–O bond length, which remains unchanged (∼1.45 Å) despite this distortion. An interaction that is primarily physisorption is further supported by the tiny Bader charge transfer (−0.04e). According to these results, which are in line with earlier findings on fully terminated MXenes and oxide surfaces, the pristine $Ti_3C_2O_2$ surface is not reactive enough to activate the peroxide O–O bond.

3.1.2 Adsorption on oxygen-deficient $Ti_3C_2O_2$–O_{vac}. It is shown that PBE + U and r^{2}SCAN differ significantly in terms of H_2O_2 adsorption at oxygen vacancy sites. Upon relaxation, H_2O_2 in PBE + U spontaneously dissociates, breaking O–O bonds and producing molecular H_2O (Fig. S1f). Significant charge transfer (1.13e) and a huge adsorption energy (−5.03 eV) define this dissociative adsorption, which suggests the typical over-binding often associated with defect states in GGA + U frameworks. However, according to r^{2}SCAN, H_2O_2 keeps the molecular adsorption state at the O_{vac} site steady (Fig. 1g). The adsorption energy (−1.60 eV) is much more modest than the PBE + U value, and the O–O bond is still intact with a length comparable to the isolated molecule. An O(H_2O_2)–Ti distance of 2.34 Å and a slight charge transfer of −0.15e support this stability, indicating a partial covalent interaction instead of electron-driven bond scission.

To verify these findings, we performed independent structural optimizations using the HSE06 hybrid functional (Fig. 1h). While r^{2}SCAN is more computationally intensive than the standard GGA + U, HSE06 carries a vastly higher computational cost, making it impractical for exhaustive screening but ideal as a high-level benchmark. A qualitatively equivalent adsorption geometry with comparable Ti–O coordination and intact O–O bonding is produced by the HSE06 results. There are two reasons for this agreement:

- Validation: it excludes the spontaneous dissociation observed in PBE + U and validates the r^{2}SCAN prediction of molecule adsorption.
- Efficiency: it shows that r^{2}SCAN effectively mitigates the self-interaction mistakes that beset less expensive GGA + U methods by capturing the complex electronic exchange–correlation effects of a hybrid functional at a quarter of the HSE06 overhead.

It has been previously recognized that semi-local DFT functionals, like PBE, have delocalization (self-interaction) errors, which can paradoxically result in inflated adsorbate binding energies and underestimated surface energies on transition-metal oxide surfaces.[55,56] These mistakes are generally reduced by hybrid functionals that contain a portion of Hartree–Fock exchange, producing adsorption energies that are weaker and frequently more physically realistic. The localization of transition-metal d electrons is improved by standard DFT + *U* corrections, but when adsorbate states are present, delocalization error is not always completely eliminated. Therefore, how the underlying functional handles electron delocalization and charge transfer in surface–adsorbate interactions may result in variations in the expected adsorption mechanisms (*e.g.*, barrierless dissociation *versus* intact adsorption) between PBE + *U* and hybrid or meta-GGA functionals.

3.1.3 Comparison between r^{2}SCAN and PBE + *U* adsorption mechanisms. According to the comparison between PBE + *U* and r^{2}SCAN, the dissociative adsorption at oxygen vacancies that PBE + *U* anticipated is probably an artifact of over-binding and inflated defect reactivity. Although oxygen vacancies do increase surface reactivity, r^{2}SCAN shows that this improvement is not sufficient to cause barrierless O–O bond breaking. As an alternative, the vacancy stabilizes a strongly bonded molecular H_2O_2 intermediate, which could serve as a prelude to later activated dissociation in thermal or electrochemical settings.

These findings demonstrate how important the exchange–correlation functional is for explaining the chemistry of peroxide on MXene surfaces. The enhanced reactivity of oxygen vacancies is qualitatively captured by PBE + *U*, whereas r^{2}SCAN avoids unphysical dissociation pathways and offers a more accurate representation of adsorption energetics and bonding. For simulating peroxide-related reaction processes on defect-engineered MXenes, r^{2}SCAN is hence more appropriate.

Overall, by showing that oxygen vacancies significantly stabilize molecular peroxide species rather than causing spontaneous dissociation, the r^{2}SCAN results improve our knowledge of H_2O_2 adsorption on $Ti_3C_2O_2$ MXene. This realization has significant implications for peroxide-mediated catalytic processes, such as advanced oxidation reactions and oxygen reduction, where it is frequently preferred to have regulated activation of H_2O_2 rather than full breakdown.

The band structures and DOS/PDOS for pristine $Ti_3C_2O_2$, H_2O_2-adsorbed $Ti_3C_2O_2$, oxygen-deficient $Ti_3C_2O_2$–O_{vac}, and H_2O_2 adsorbed at the $Ti_3C_2O_2$–O_{vac} are shown in Fig. 2a–h. The system has an ultranarrow band gap of around 0.002 eV and a virtually metallic character[57–59] for clean $Ti_3C_2O_2$ (Fig. 2a). Recent research has also revealed that $Ti_3C_2O_2$ may behave like an excitonic insulator in specific situations, further highlighting its unusual electrical characteristics.[60] In accordance with the well-established metallic character of Ti-based MXenes and strong Ti–C/Ti–O hybridization, Ti 3d orbitals dominate the states close to the Fermi level, whereas C 2p and O 2p states primarily occupy the lower valence region (Fig. 2b).

The introduction of an oxygen vacancy (Fig. 2c and d) slightly modifies the electronic structure, while preserving the quasi-metallic character (band gap $\sim$ 0.003 eV). The presence of coordinatively unsaturated Ti atoms and localized defect-related states is reflected in the slight changes in the Ti 3d manifold caused by the vacancy, especially in the vicinity of the Fermi level. These states do not, however, create a significant gap and are nevertheless highly hybridized with the MXene framework. The O p orbital contribution is represented by the red-colored curve in Fig. 2b (PDOS), whereas the Ti d states are represented by the blue-colored curve. The pristine system's metallic-like behavior is confirmed by the PDOS, which unequivocally shows that Ti d orbitals contribute the majority of the electronic states close to the Fermi level. On the other hand, the red line in Fig. 2d (TDOS comparison) represents the overall density of states of pristine $Ti_3C_2O_2$. The oxygen-defective system is represented by the blue curve in this panel.

The overall band dispersion and DOS are essentially unaffected by the molecule adsorption of H_2O_2 on the clean surface (Fig. 2e and f), but the band gap slightly increases to $\sim$0.003 eV. Weak electronic disruption of the MXene substrate is indicated by the DOS, which does not reveal the creation of new mid-gap states or substantial redistribution close to the Fermi level. This behavior aligns with the molecularly intact adsorption shape seen in the optimized structure and is compatible with hydrogen bonding-dominated physisorption.

The band gap narrows to about 0.001 eV when H_2O_2 adsorbs at the oxygen-vacancy site (Fig. 2g and h), and there is a noticeable increase in Ti 3d contributions close to the Fermi level. Crucially, the overall DOS profile closely resembles that of the defective surface, and no isolated peroxide-derived states are visible within the gap region. This suggests that the unsaturated Ti centers and H_2O_2 have a strong electronic connection without excessive charge localization into antibonding peroxide orbitals. The r^{2}SCAN- and HSE06-optimized geometries, which both stabilize molecular H_2O_2 adsorption without O–O bond cleavage at the vacancy site, are compatible with the lack of mid-gap states and substantial DOS reshaping.

Overall, the r^{2}SCAN electronic-structure results show that oxygen vacancies maintain a physically plausible description of peroxide bonding while improving surface reactivity mainly by raising Ti 3d density close to the Fermi level, which promotes stronger adsorbate–substrate interaction. This shows the better balance between metal–oxygen coordination and intramolecular peroxide stability attained by r^{2}SCAN, in contrast to PBE + *U* predictions of spontaneous dissociation.

3.2 Electron localization function (ELF) analysis

At the r^{2}SCAN level of theory, ELF calculations were carried out to clarify the nature of charge redistribution and chemical bonding for H_2O_2 adsorbed on the $Ti_3C_2O_2$/$Ti_3C_2O_2$–O_{vac} surface. Values near 1 (red) suggest highly localized electron density linked to covalent bonds or lone pairs, whereas values near 0 (blue) indicate electron depletion or delocalized metallic bonding. ELF offers a real-space picture of electron localization. This analysis is especially helpful for determining the degree of electronic coupling with coordinatively unsaturated Ti atoms at vacancy sites and the integrity of the peroxide O–O bond.

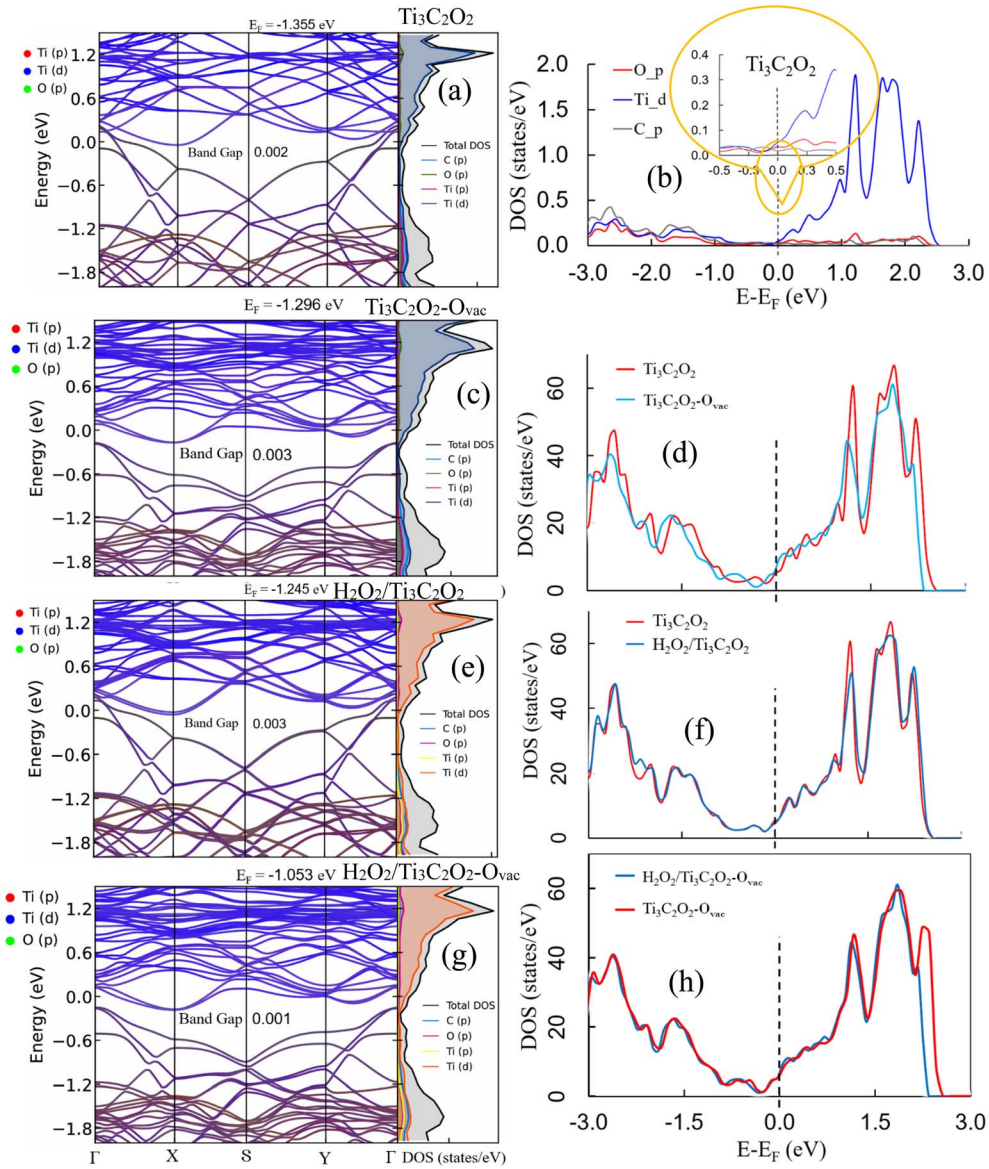

Fig. 2 Electronic structure analysis of pristine $Ti_3C_2O_2$, oxygen-vacant $Ti_3C_2O_2$ ($Ti_3C_2O_2$–O_{vac}), and H_2O_2 adsorbed surfaces. (a, c, e and g) Calculated energy band structures along the high-symmetry paths of the Brillouin zone and corresponding Total Density of States (TDOS) for (a) pristine $Ti_3C_2O_2$, (c) $Ti_3C_2O_2$–O_{vac}, (e) $H_2O_2/Ti_3C_2O_2$, and (g) $H_2O_2/Ti_3C_2O_2$–O_{vac}. The Fermi level (E_F) is aligned at 0 eV (indicated by the dashed horizontal line), with calculated band gap values as the inset text. (b) Projected Density of States (PDOS) for the O p, Ti d, and C p orbitals of pristine $Ti_3C_2O_2$, highlighting the electronic contributions near the Fermi level (magnified inset). (d, f and h) Comparative TDOS plots showing the electronic shifts upon modification: (d) comparison between pristine $Ti_3C_2O_2$ and oxygen-vacant $Ti_3C_2O_2$–O_{vac}. (f) Comparison between pristine $Ti_3C_2O_2$ and the H_2O_2 adsorbed surface. (h) Comparison between the oxygen-vacant surface before and after H_2O_2 adsorption.

The ELF map for H_2O_2 adsorbed at the $Ti_3C_2O_2$ and $Ti_3C_2O_2$–O_{vac}, as illustrated in Fig. 3, shows a prominent red localization region between the two oxygen atoms, indicating that a strong covalent O–O bond has been preserved. The fact that the equivalent O–O bond length stays near that of the free H_2O_2 molecule suggests that adsorption does not induce significant bond elongation or activation toward dissociation. In keeping with the localized lone-pair electron density typical of molecular peroxide species, distinct red lobes are also seen around each oxygen atom.

The ELF shows moderate green to yellow localization between the exposed Ti centers at the vacancy site and the peroxide oxygen atoms in the interfacial region between H_2O_2 and the defective $Ti_3C_2O_2$ surface. Strong adsorbate–substrate contact without significant charge transfer into the peroxide antibonding orbitals is indicated by the development of partly covalent Ti–O coordination bonds. Crucially, unlike what would be anticipated for a weakened or broken O–O bond, the interatomic area between the two oxygen atoms does not exhibit any blue (electron-depleted) feature. Additionally, there is no indication of proton transfer or rehybridization, and the ELF distribution surrounding the hydrogen atoms of H_2O_2 is essentially unaltered during adsorption. This implies that the molecule stays intact on the surface and that O–H bonds are

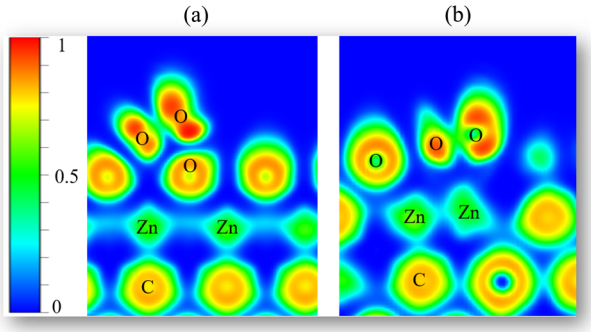

Fig. 3 Electron Localization Function (ELF) analysis of adsorbed H_2O_2 on (a) pristine and (b) O-vacancy defective $Ti_3C_2O_2$ using the r^{2}SCAN method (color scale: red = highly localized electrons, blue = electron-depleted regions).

maintained. A balanced description of metal–oxygen coordination and intramolecular peroxide bonding is provided by r^{2}SCAN, as evidenced by the lack of notable electron depletion along the O–O axis.

Overall, even in the presence of extremely reactive vacancy sites, the r^{2}SCAN-based ELF analysis clearly shows that H_2O_2 adsorbs molecularly on the oxygen-deficient $Ti_3C_2O_2$ surface. By accepting electron density into Ti–O coordination bonds, the exposed Ti atoms improve adsorption without weakening the peroxide O–O bond. This result contrasts with PBE + U predictions of spontaneous dissociation and is entirely compatible with the geometries optimized by r^{2}SCAN and HSE06, demonstrating the enhanced physical reliability of r^{2}SCAN for characterizing defect-mediated peroxide adsorption on MXene surfaces.

3.3 Reaction pathway and dissociation kinetics from CI-NEB analysis

To study the dissociation of H_2O_2 and the potential mechanism of H_2O generation on oxygen-defective $Ti_3C_2O_2$, the CI-NEB approach based on the MLIP-CHGNet framework was used. The CI-NEB calculations were intended to clarify the minimum-energy reaction pathway for peroxide activation and dissociation at an oxygen vacancy site. The $H_2O_2/Ti_3C_2O_2$–O_{vac} system was optimized using CHGNet in order to evaluate the dependability of the MLIP-CHGNet approach for structural optimization. The optimized bond lengths (Fig. 4a) closely match the r^{2}SCAN and HSE06 values, and no spontaneous O–O dissociation is seen during adsorption, suggesting that CHGNet effectively captures the important interfacial interactions in the system under study.

A multi-step dissociation process with two unique activation barriers, E_a(I) and E_a(II), with remarkably low magnitudes of 0.01 eV and 0.07 eV, respectively, is shown by the predicted reaction pathway (Fig. 4b). These low barriers suggest that an extremely favorable environment for H_2O_2 activation is provided by oxygen-defective $Ti_3C_2O_2$.

The first activation barrier (E_a(I)) corresponds to a structural rearrangement of the adsorbed H_2O_2 molecule rather than O–O bond cleavage. H_2O_2 modifies its adsorption configuration at the vacancy site along the early stages of the reaction coordinate, as shown in Fig. 4c (steps 1–3). This is followed by minor modifications in the interaction between one peroxide oxygen ($O(H_2O_2)$) and the exposed Ti atoms. In particular, the O–O bond length generally stays the same between stages 2 and 3, although the $O(H_2O_2)$–Ti distance increases marginally from 2.486 Å to 2.494 Å. This demonstrates that rather than chemical bond breakage, E_a(I) results from peroxide reorientation and electronic polarization brought on by the defect location.

Peroxide dissociation starts when the O–O bond starts to elongate considerably between stages 4 and 5. Interestingly, the total energy of the system falls (energetically more stable state) even if the O–O bond weakens. The dissociating oxygen species and the vacancy-exposed Ti atoms form strong Ti–O coordination bonds with Ti–O bond lengths of about 2.18 Å, which is what causes this stabilization. The reaction pathway has a deep local minimum because of the strong metal–oxygen interaction, which offsets the energy cost of O–O bond breaking.

A comparable stabilizing impact is seen between steps 13 and 14 farther down the pipeline. Although this segment involves elongation of both the $O(H_2O_2)$–Ti bond and the hydrogen bond between the emerging H_2O molecule and surface oxygen, the system remains energetically favorable. The significant shortening of the Ti–O bond from 2.336 Å to 2.080 Å indicates that the $O(H_2O_2)$ fragment becomes more firmly integrated into the $Ti_3C_2O_2$ lattice, hence reducing the system's total energy.

The final separation of reaction products from the surface, as opposed to bond cleavage, is linked to the second activation barrier (E_a(II)), which happens between steps 14 and 15. The formation and partial desorption of an H_2O molecule away from the $Ti_3C_2O_2$ surface is correlated with this barrier. This step's structural characteristics include a significant elongation of the $O(H_2O_2)$–Ti bond from 2.509 Å to 2.635 Å and the hydrogen bond between H_2O and surface oxygen weakening from 2.355 Å to 3.086 Å. The second, though still tiny, activation barrier is caused by the loss of significant surface stability during this phase.

According to the CI-NEB data, H_2O_2 dissociation on oxygen-defective $Ti_3C_2O_2$ occurs in a sequential, surface-stabilized manner with remarkably low kinetic barriers. While the first barrier reflects electronic polarization and molecular rearrangement, the second barrier is associated with product detachment rather than bond breakage. Because the exposed Ti atoms function as potent electron-accepting centers that stabilize dissociation intermediates through strong Ti–O bonding, the oxygen vacancy is essential.

Note that CI-NEB calculations inherently depict reaction pathways under static conditions at 0 K (isolated system). At room temperature, where thermal fluctuations and entropic contributions may further accelerate bond breaking and product diffusion, H_2O_2 dissociation should be easily accessible due to the incredibly low activation energies found here. Future work will address the need for *ab initio* or machine-learning-based MD simulations to completely capture these finite-

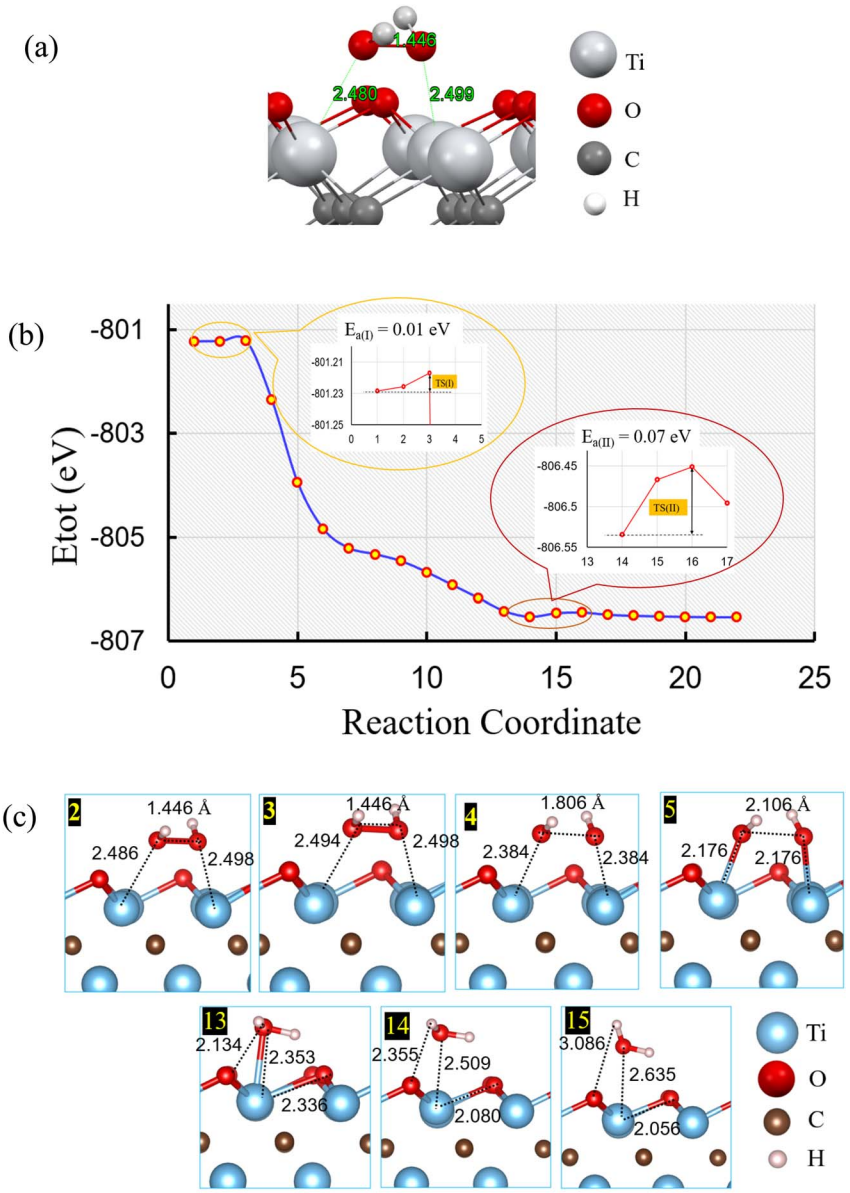

Fig. 4 (a) The optimized structure of the initial configuration (reactant) for the $H_2O_2/Ti_3C_2O_2$ system with MLIP-CHGNet. (b) CI-NEB energy profile for H_2O_2 dissociation on oxygen-deficient $Ti_3C_2O_2$ ($Ti_3C_2O_2$–O_{vac}) obtained using the CHGNet machine-learned interatomic potential. The reaction proceeds *via* a two-step mechanism with very low activation barriers of E_a(I) ≈ 0.01 eV and E_a(II) ≈ 0.07 eV. The first barrier corresponds to peroxide reorientation at the vacancy site, while the second is related to product separation and H_2O formation. Insets indicate the corresponding transition states. (c) Selected intermediate structures along the reaction pathway showing the evolution of key bond distances. The images illustrate molecular adsorption, O–O bond elongation and cleavage, stabilization of dissociation intermediates through strong Ti–O coordination, and final H_2O formation at the defect site.

temperature effects and evaluate the dynamical stability of reaction intermediates.

3.4 MLIP-MD simulation of H_2O_2 on $Ti_3C_2O_2$–O_{vac} under ambient conditions

The dynamic effects of thermal fluctuations, solvation, and entropic contributions that control catalytic behavior under realistic conditions are not fully captured by static geometry optimizations and CI-NEB calculations, even though they offer crucial insight into intrinsic adsorption configurations and minimum-energy reaction pathways. To bridge this gap, MLIP-MD simulations were carried out utilizing the CHGNet potential in the Janus framework. This allowed for an atomistic description of H_2O_2 adsorption and possible dissociation on O-vacancy $Ti_3C_2O_2$ in both aqueous and ambient-like settings. This method enables direct evaluation of the viability of peroxide activation over the assumed 0 K limit as well as the thermal stability of adsorbed intermediates.

3.4.1 MLIP-MD simulation of $H_2O_2/Ti_3C_2O_2$–O_{vac} at zero K.

Prior to investigating finite-temperature effects, zero K (Fig. S2a) structural optimizations of the $H_2O_2/Ti_3C_2O_2$–O_{vac} system utilizing the CHGNet potential was used to evaluate the

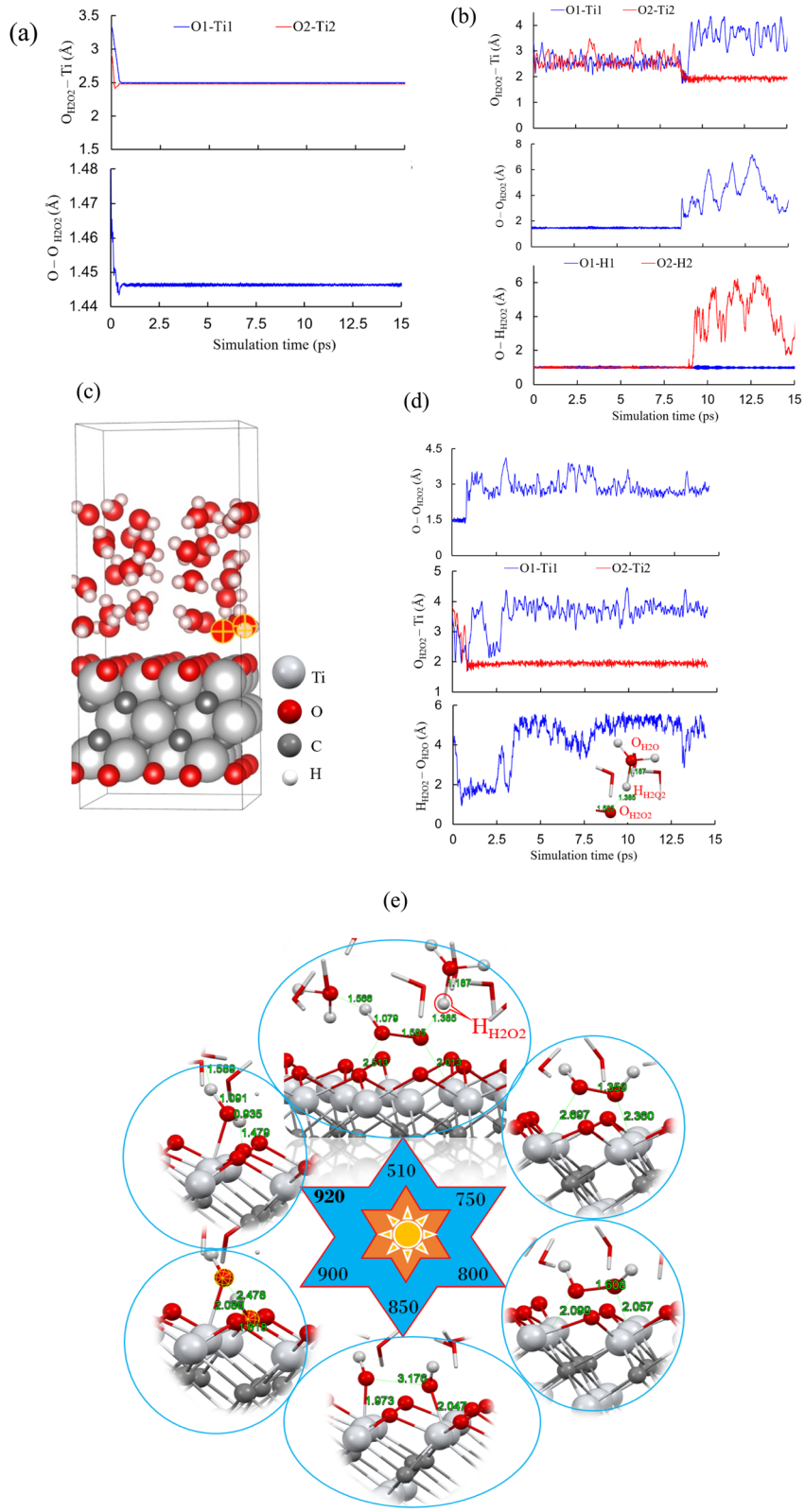

Fig. 5 CHGNet/MLIP-MD simulations of H_2O_2 adsorption and dissociation on oxygen-deficient $Ti_3C_2O_2$ ($Ti_3C_2O_2$–O_{vac}). (a) Time evolution of O(H_2O_2)–Ti and O–O bond distances at 0 K, confirming stable molecular adsorption and preservation of the peroxide bond. (b) Bond-distance analysis at 300 K showing thermally activated O–O bond cleavage, defect-site coordination of oxygen atoms, and formation of surface-bound intermediates. (c) Initial model of the H_2O + H_2O_2/$Ti_3C_2O_2$–O_{vac} system (explicit aqueous environment) used in the MLIP-MD simulations. (d) The time evolution of O–O, O(H_2O_2)–Ti, and H–O distances indicates spontaneous peroxide dissociation, formation of surface hydroxyl species, and stabilization of reaction intermediates through hydrogen bonding and proton transfer within the surrounding water network. (e) MLIP-MD simulation of H_2O_2 on $Ti_3C_2O_2$–O_{vac} in an explicit aqueous environment.

accuracy of the MLIP-MD framework. In order to directly compare these calculations with the DFT-level geometries discussed in Sections 3.1–3.3, they were carried out to simulate an isolated, static system.

As illustrated in Fig. 5a, the optimized MLIP-MD structure exhibits no O–O bond dissociation upon adsorption, preserving the molecular integrity of H_2O_2 at the vacancy site. While clearly deviating from the PBE + *U* predictions that tend to overactivate the peroxide molecule, the important interfacial bonding distances, especially the O(H_2O_2)–Ti distances, are in close quantitative agreement with those derived at the r^{2}SCAN and HSE06 levels of theory. This agreement demonstrates that the potential energy surface controlling H_2O_2 adsorption on defective $Ti_3C_2O_2$ at 0 K is accurately reproduced by the MLIP-MD/CHGNet system.

Further evidence that the adsorbed molecular configuration is stable throughout the zero K relaxation is provided by the temporal history of representative O–O lengths (Fig. 5a), which shows no indication of O–O bond elongation toward dissociation and just slight variations around equilibrium values. These outcomes support the usage of MLIP-MD optimized geometries as trustworthy foundations for ensuing reaction pathway studies and finite-temperature molecular dynamics simulations.

3.4.2 MLIP-MD simulation of $H_2O_2/Ti_3C_2O_2$–O_{vac} at 300 K. In order to evaluate the impact of thermal effects on the reactivity of the $H_2O_2/Ti_3C_2O_2$–O_{vac} system, finite-temperature MLIP-MD simulations were conducted using the CHGNet potential in the Janus framework at 300 K, which represents ambient conditions. By explicitly accounting for thermal fluctuations and dynamical bond rearrangements, our simulations allow for a direct assessment of whether peroxide dissociation may be thermally activated on the defective MXene surface, in contrast to the zero K optimizations previously addressed.

The equilibration behavior of the system is displayed in Fig. S2b, where the temperature quickly approaches and then steadily varies around 300 K throughout the simulation time, demonstrating that the MLIP-MD framework produces a well-equilibrated canonical (NVT) ensemble. The lack of significant temperature drifts or instabilities is significant because it suggests that intrinsic response dynamics, not numerical distortions or inadequate thermostating, are the cause of the observed structural and energetic changes. During the MD trajectory, the total energy simultaneously shows a stepwise decrease, signaling discrete structural transformations instead of straightforward thermal fluctuations.

The underlying reaction mechanism may be directly inferred from the evolution of important bonding lengths throughout the MD trajectory (Fig. 5b). At the beginning of the simulation, the O(H_2O_2)–Ti distances oscillate around values similar to those measured at 0 K and at the r^{2}SCAN/HSE06 levels, suggesting that H_2O_2 is still molecularly adsorbed. The O–O bond in H_2O_2 is seen to elongate significantly as the dynamics progress, and the O(H_2O_2)–Ti bond is also strengthened. At a finite temperature, this cooperative bond evolution signals the onset of peroxide activation. The O–O bond irreversibly ruptures however at later simulation times, which also happen to be when the total energy sharply stabilizes. Concurrently, one oxygen atom from H_2O_2 fills the vacancy site, repairing the surface defect, and the remaining OH fragment joins hydrogen to form a molecular H_2O species, which slowly separates off the surface. The completion of the dissociation process and product production is verified by the elongation of the O(H_2O_2)–Ti distance after dissociation and the stabilization of the O–O distance in the newly formed H_2O molecule.

Due to the coordinatively unsaturated surface metal atoms, the O-vacancy defect serves as a highly reactive adsorption center. This defect introduces localized electronic states near the Fermi level, in contrast to pristine O-terminated MXene surfaces where H_2O_2 is physisorbed. By facilitating σ-donation from the O–O lone pairs and subsequent back-donation into the antibonding σ* orbitals of H_2O_2, these states stabilize the peroxide approach, acting simultaneously as electron donors and acceptors.[61–64]

The elongation of the peroxide bond, which begins at 8.75 ps (from about 1.45 Å to approximately 2.5 Å), is a result of the pre-activation of the O–O bond caused by this electronic interaction. The beginning of chemisorption is indicated by the simultaneous drop in the surface metal–oxygen interaction distances (from approximately 2.5 Å to approximately 1.9 Å).

These finite-temperature MLIP-MD results show that, even if H_2O_2 is still molecularly adsorbed at 0 K, the minor kinetic barriers found in the CI-NEB study can be overcome by thermal activation at room temperature, allowing for spontaneous dissociation. Temperature plays a crucial role in activating peroxide chemistry on defective $Ti_3C_2O_2$ MXene, as evidenced by the observed step-wise energy reduction and coordinated bond rearrangements. When combined, the zero K and 300 K MLIP-MD simulations provide a consistent mechanistic picture: O–O bond cleavage, defect filling, and H_2O formation are driven by thermal fluctuations at room temperature, which explains the experimentally relevant reactivity under ambient conditions, while vacancy-exposed Ti sites stabilize molecular H_2O_2 under isolated conditions.

3.4.3 MLIP-MD simulation of $H_2O_2/Ti_3C_2O_2$–O_{vac} in an aqueous environment at 300 K. In order to clarify the impact of solvent effects on H_2O_2 reactivity, MLIP-MD simulations were expanded to an explicit aqueous environment, by adding many water molecules ($n$$H_2O$ + $H_2O_2/Ti_3C_2O_2$–O_{vac} (Fig. 5c)). This configuration allows direct evaluation of hydrogen-bonding networks, proton transfer events, and solvent-assisted reaction pathways under ambient conditions (300 K), which is more representative of realistic catalytic environments than isolated or vacuum circumstances. Stable temperature fluctuations around 300 K and a slow, stepwise decrease in total energy demonstrate that the aqueous system quickly reaches thermal and energetic equilibrium (Fig. S2c). This energy stabilization validates the robustness of the MLIP-MD description for long-time dynamics in liquid water and shows that unphysical structural drift is absent.

Fig. 5d summarizes the time evolution of important interatomic distances during the MD simulation. In stark contrast to the vacuum MD results at 300 K—where the O–O bond in H_2O_2 remained intact over the simulation timescale (at 8.75 ps)—the

O–O distance in aqueous media increases sharply at the very early stages of the simulation (at 0.80 ps), indicating prompt O–O bond dissociation. This finding shows that the effective kinetic barrier for peroxide breakdown is significantly reduced when surrounding water molecules are present.

Both oxygen atoms of H_2O_2 initially interact with the under-coordinated Ti sites at the vacancy, but after dissociation, one of them gradually moves away from the surface while the other becomes strongly incorporated into the defective $Ti_3C_2O_2$ lattice, according to the O(H_2O_2)–Ti distances. This behavior is consistent with defect healing, which results in a more stable surface configuration when an oxygen atom from H_2O_2 fills the vacancy.

The dynamic evolution of H(H_2O_2)–O(H_2O) distances is a crucial characteristic that is exclusive to the aqueous system (Fig. 5d). Throughout the simulation, these distances significantly decrease, suggesting that H_2O_2 and the nearby water molecules are actively transferring hydrogen. Rapid proton shuttling is made possible by hydrogen bonding throughout the water network in this process, which reflects a Grotthuss-like proton relay mechanism.[65–67] By stabilizing transient hydroxyl species and promoting the synthesis of molecular H_2O, this solvent-mediated hydrogen transfer successfully combines proton redistribution and O–O bond cleavage. This process demonstrates the catalytic function of the hydrogen-bond network in reducing kinetic limitations and explains why H_2O_2 dissociates in water much more quickly than under vacuum.

A schematic representation of the H_2O_2 adsorption and dissociation process in an aqueous environment is shown in Fig. 5e. At the O-vacancy site, H_2O_2 first adsorbs *via* robust Ti–O interactions. The O–O bond is quickly destabilized by the combined effects of solvent-assisted proton transfer and vacancy-induced electronic activation, which causes early separation. One oxygen atom fills the surface vacancy, while the remaining fragments culminate in the formation of the H_2O molecule. Furthermore, according to the dynamical simulations, the oxygen species produced during dissociation are still chemically active and can take part in redox or protonation events that can renew oxygen vacancies (Fig. 5e). Therefore, rather than being an irreversible structural change, the vacancy-healing effect is temporary and a component of a dynamic catalytic cycle. It is anticipated that under practical operating conditions, this reversible defect chemistry will sustain catalytic performance.

As a whole, these MLIP-MD results show that the kinetics and mechanism of H_2O_2 breakdown on $Ti_3C_2O_2$–O_{vac} are significantly changed by explicit water molecules. Aqueous media facilitate proton-coupled reaction pathways that are unavailable in isolated systems and speed up O–O bond breakage as compared to vacuum conditions. This highlights the necessity of incorporating explicit solvent effects when evaluating the catalytic performance of MXene-based materials under realistic operating conditions.

4. Conclusion

In this work, we have used an integrated framework that combines DFT calculations and MLIP-MD simulations to clarify the adsorption, activation, and dissociation mechanisms of hydrogen peroxide on pristine and oxygen-defective $Ti_3C_2O_2$ MXene. By systematically comparing PBE + *U*, r^{2}SCAN, and HSE06 levels of theory, we demonstrate that meta-GGA and hybrid functionals provide a more physically reliable description of peroxide–MXene interactions, particularly at oxygen vacancy sites where self-interaction errors can otherwise lead to artificial overbinding and barrierless dissociation.

According to our findings, pristine $Ti_2C_2O_2$ supports only weak molecule adsorption without O–O bond activation, acting as a mostly inert substrate toward H_2O_2. On the other hand, oxygen vacancies create coordinatively unsaturated Ti centers that stabilize a molecular peroxide intermediate and firmly bind H_2O_2. ELF analysis, which shows preserved O–O covalent bonding together with partially covalent Ti–O coordination, further supports the idea that this intermediate is unaffected by zero temperature, as confirmed by r^{2}SCAN and HSE06 calculations.

An energetically favorable, multi-step dissociation process with ultralow activation barriers is revealed by CI-NEB calculations using the MLIP-CHGNet framework. This suggests that oxygen vacancies significantly reduce the kinetic threshold for peroxide activation. Crucially, MLIP-MD simulations at 300 K in an explicit aquatic environment extend these static 0 K results to actual settings. The finite-temperature simulations show that surrounding water molecules and thermal fluctuations are critical for promoting proton transfer *via* hydrogen-bond networks, stabilizing charged and polar intermediates, and aiding O–O bond cleavage. This highlights the cooperative interaction between surface defects and solvent dynamics, as peroxide dissociation happens much more quickly in water than in isolated or vacuum settings.

Furthermore, it emphasizes that in order to replicate genuine reaction mechanisms, finite-temperature, explicitly solvated MLIP-MD simulations must be combined with precise exchange–correlation functionals. These insights offer a strong theoretical basis for the rational design of MXene-based catalysts for environmental and peroxide-mediated electrochemical applications.

Conflicts of interest

There are no conflicts to declare.

Data availability

All data supporting the findings of this study are included within the article.

Supplementary information (SI): optimized geometric parameters for pristine and defective MXene surfaces, H_2O_2 adsorption configurations, and MLIP-MD equilibration profiles for vacuum and aqueous interfaces. See DOI: https://doi.org/10.1039/d5na00962f.

Acknowledgements

This study was supported by the Virtual Engineering Platform Project (Grant No. P0022336), funded by the Ministry of Trade, Industry & Energy (MoTIE, South Korea).

References

1 C. M. Lousada, A. J. Johansson, T. Brinck and M. Jonsson, *J. Phys. Chem. C*, 2012, **116**, 9533.
2 X. Jiao, H. Song, H. Zhao, W. Bai, L. Zhang and Y. Lv, *Anal. Methods*, 2012, **4**, 3261.
3 J. Takagi and K. Ishigure, *Nucl. Sci. Eng.*, 1985, **89**, 177.
4 H. A. Hiroki and J. A. LaVerne, *J. Phys. Chem. B*, 2005, **109**, 3364.
5 T. Pirmohamed, *et al.*, *Chem. Commun.*, 2010, **46**, 2736.
6 W.-F. Huang, P. Raghunath and M. C. Lin, *J. Comput. Chem.*, 2011, **32**, 1065.
7 L. Wang, J. Zhang, Y. Zhang, H. Yu, Y. Qu and J. Yu, *Small*, 2021, 2104561.
8 Z. Li, J. Sheng, Y. Zhang, X. Li and Y. Xu, *Appl. Catal., B*, 2015, **166–167**, 313.
9 A. M. Baker, S. M. Stewart, K. P. Ramaiyan, D. Banham, S. Ye, F. Garzon, R. Mukundan and R. L. Borup, *J. Electrochem. Soc.*, 2021, **168**, 024507.
10 G. Wang, J. Zhang, X. He, Z. Zhang and Y. Zhao, *Chin. J. Chem.*, 2017, **35**, 791.
11 R. Fiorenza, S. A. Balsamo, L. D'Urso, S. Sciré, M. V. Brundo, R. Pecoraro, E. M. Scalisi, V. Privitera and G. Impellizzeri, *Catalysts*, 2020, **10**, 446.
12 N. M. Markovic and P. N. Ross, *Surf. Sci. Rep.*, 2002, **45**, 117.
13 B. C. H Steele and A. Heinzel, *Nature*, 2001, **414**, 345.
14 R. Adzic, in *Electrocatalysis*, ed. J. Lipkowski and P. N. Ross, Wiley-VCH, New York, 1998, pp. 197–242.
15 A. B. Anderson and T. V. Albu, *J. Electrochem. Soc.*, 2000, **147**, 4229.
16 A. B. Anderson, J. Roques, S. Mukerjee, V. S. Murthi, N. M. Markovic and V. Stamenkovic, *J. Phys. Chem. B*, 2005, **109**, 1198.
17 P. B. Balbuena, S. R. Calvo, E. J. Lamas, P. F. Salazar and J. M. Seminario, *J. Phys. Chem. B*, 2006, **110**, 17452.
18 K. R. G. Lim, M. Shekhirev, B. C. Wyatt, B. Anasori, Y. Gogotsi and Z. W. She, *Nat. Synth.*, 2022, **1**, 601.
19 M. Khazaei, A. Mishra, N. S. Venkataramanan, A. K. Singh and S. Yunoki, *Curr. Opin. Solid State Mater. Sci.*, 2019, **23**, 164.
20 H. Li, J. Hou, Q. Duan, L. Meng, F. Viñes and F. Illas, *ChemPhysChem*, 2025, **25**, e2500099.
21 N. Liu, Q. Li, H. Wan, *et al.*, *Nat. Commun.*, 2022, **13**, 5551.
22 M. Magnuson, P. Eklund and C. Polley, *Phys. Rev. Lett.*, 2025, **134**, 106201.
23 A. V. Mohammadi, *et al.*, *ACS Nano*, 2017, **11**, 11135.
24 M. R. Lukatskaya, *et al.*, *Science*, 2013, **341**, 1502.
25 B. Anasori, M. R. Lukatskaya and Y. Gogotsi, *Nat. Rev. Mater.*, 2017, **2**, 16098.
26 M. Khazaei, *et al.*, *Adv. Funct. Mater.*, 2013, **23**, 2185.
27 J. D. Gouveia, Á. Morales-García, F. Viñes, F. Illas and J. R. B. Gomes, *Appl. Catal., B*, 2020, **260**, 118191.
28 J. Guo, *et al.*, *ACS Nano*, 2021, **15**, 7237.
29 T. Ma, *et al.*, *Nano Energy*, 2022, **93**, 106849.
30 X. Wu, *et al.*, *Adv. Sci.*, 2021, **8**, 2100935.
31 M. Kolos and F. Karlický, *JPhys Mater.*, 2025, **8**, 035001.
32 X. Chen, *et al.*, *Surf. Sci. Rep.*, 2019, **74**, 291.
33 J. P. Perdew and A. Zunger, *Phys. Rev. B:Condens. Matter Mater. Phys.*, 1981, **23**, 5048.
34 A. J. Cohen, P. Mori-Sánchez and W. Yang, *Science*, 2008, **321**, 792.
35 D. Marx and J. Hutter, *Ab initio Molecular Dynamics: Basic Theory and Advanced Methods*, Cambridge University Press, 2009.
36 M. E. Tuckerman, *Statistical Mechanics: Theory and Molecular Simulation*, Oxford University Press, 2010.
37 J. Sun, A. Ruzsinszky and J. P. Perdew, *Phys. Rev. Lett.*, 2015, **115**, 036402.
38 J. Heyd, G. E. Scuseria and M. Ernzerhof, *J. Chem. Phys.*, 2003, **118**, 8207.
39 J. Behler and M. Parrinello, *Phys. Rev. Lett.*, 2007, **98**, 146401.
40 B. Deng, *et al.*, *npj Comput. Mater.*, 2023, **9**, 15.
41 G. Piccini, M. Lee, S. F. Yuk, D. Zhang, G. Collinge, L. Kollias, M. Nguyen, V. Glezakou and R. Rousseau, *Catal. Sci. Technol.*, 2022, **12**, 12.
42 Y. Han, H. Xu, Q. Li, A. Du and X. Yan, *Front. Chem.*, 2023, **11**, 1286257.
43 B. Sun, H. Liu, H. Song, G. Zhang, H. Zheng and X.-G. Zhao, *J. Chem. Phys.*, 2014, **140**, 164709.
44 G. Kresse and J. Furthmüller, *Comput. Mater. Sci.*, 1996, **6**, 15.
45 G. Kresse and J. Furthmüller, *Phys. Rev. B:Condens. Matter Mater. Phys.*, 1996, **54**, 11169.
46 G. Kresse and D. Joubert, *Phys. Rev. B:Condens. Matter Mater. Phys.*, 1999, **59**, 1758.
47 J. P. Perdew, K. Burke and M. Ernzerhof, *Phys. Rev. Lett.*, 1996, **77**, 3865.
48 B. Himmetoglu, *et al.*, *Int. J. Quantum Chem.*, 2014, **114**, 14.
49 T. Sakhraoui and F. Karlický, *ACS Omega*, 2022, **7**, 42221.
50 A. Hjorth Larsen, *J. Phys.: Condens. Matter*, 2017, **29**, 273002.
51 D. Wines, *et al.*, *Appl. Phys. Rev.*, 2023, **10**, 041302.
52 K. Choudhary, *npj Comput. Mater.*, 2020, **6**, 173.
53 E. Kasoar, *et al.*, *Janus-Core, Machine Learning Interatomic Potentials (MLIP) Tool, v0.7.4*, 2026.
54 P. Falun, *et al.*, *J. Phys. Chem. C*, 2024, **128**, 10774.
55 Q. Zhao and H. J. Kulik, *J. Phys. Chem. Lett.*, 2019, **10**, 5090.
56 A. Bajaj and H. J. Kulik, *J. Chem. Theory Comput.*, 2022, **18**, 1142.
57 O. Mashtalir, M. Naguib, V. N. Mochalin, Y. Dall'Agnese, M. Heon, M. W. Barsoum and Y. Gogotsi, *Nat. Commun.*, 2013, **4**, 1716.
58 C. Shi, M. Beidaghi, M. Naguib, O. Mashtalir, Y. Gogotsi and S. J. L. Billinge, *Phys. Rev. Lett.*, 2014, **112**, 125501.
59 S. K. Azadi, M. Zeynali, S. Asgharizadeh and M. A. Fooladloo, *Mater. Today Commun.*, 2023, **35**, 106136.

60 N. Kumar and F. Karlický, *Appl. Phys. Lett.*, 2023, **122**, 183102.
61 R. K. Rai, A. Islam, R. S. Pati and G. Roy, *Chem.–Eur. J.*, 2025, **31**, e202403483.
62 A. Malashevich, M. Jain and S. G. Louie, *Phys. Rev. B:Condens. Matter Mater. Phys.*, 2014, **89**, 075205.
63 X.-Y. Zhang and X.-S. Chen, *Phys. Rev. Mater.*, 2019, **3**, 092801.
64 W. F. Huang, P. Raghunath and M. C. Lin, *J. Comput. Chem.*, 2011, **32**, 1065.
65 N. Agmon, *Chem. Phys. Lett.*, 1995, **244**, 456.
66 T. C. Berkelbach, H.-S. Lee and M. E. Tuckerman, *Phys. Rev. Lett.*, 2009, **103**, 238302.
67 J. H. Chen, W. T. Li, K. Y. Cai, *et al.*, *Nat. Commun.*, 2025, **16**, 3789.